Obrabotka metallov (tekhnologiya, oborudovanie, instrumenty) = Metal Working and Material Science. 2024 vol. 26 no. 3 pp. 163–178
ISSN: 1994-6309 (print) / 2541-819X (online)
DOI: 10.17212/1994-6309-2024-26.3-163-178

NSTU NETI

Obrabotka metallov -
Metal Working and Material Science

Journal homepage: http://journals.nstu.ru/obrabotka_metallov

Corrosion properties of CuAl9Mn2/ER 321 composites formed by dual-wire-feed electron beam additive manufacturing

Viktor Semin [a], ***Aleksander Panfilov*** [b], ***Veronika Utyaganova*** [c], ***Andrey Vorontsov*** [d], ***Anna Zykova*** [e, *]

Institute of Strength Physics and Materials Sciences SB RAS, 2/4, pr. Akademicheskii, Tomsk, 634055, Russian Federation

[a] https://orcid.org/0000-0003-0410-3667, viktor.semin.tsk@gmail.com; [b] https://orcid.org/0000-0001-8648-0743, alexpl@ispms.ru;
[c] https://orcid.org/0000-0002-2303-8015, veronika_ru@ispms.ru; [d] https://orcid.org/0000-0002-4334-7616, vav@ispms.ru;
[e] https://orcid.org/0000-0001-8779-3784, zykovaap@mail.ru

ARTICLE INFO

Article history:
Received: 18 April 2024
Revised: 15 May 2024
Accepted: 01 June 2024
Available online: 15 September 2024

Keywords:
Aluminum bronze
Stainless steel
Electron Beam Additive Manufacturing
Composite
Corrosion

Funding
The work was performed according to the Government research assignment for ISPMS SB RAS, project FWRW-2024-0001.

ABSTRACT

Introduction. The development of novel materials based on copper alloys and stainless steel, as well as the determination of the optimal parameters for its processing make it possible to expand the area of its implementation, increase efficiency and service life of tools and constructions. The load-bearing parts of marine equipment (bearing constructions, piston cylinders, pumps, valves, gears, rotary instruments, etc.), made of austenitic steels or aluminum bronze, are in direct contact with sea water, so the problem of increasing its corrosion resistance in the presence of strong oxidizing agents (*Cl*–, *F*– anions) is relevant. One of the advanced and actively researched methods for producing copper/steel composites is additive manufacturing that allow fabricating complex parts through layer-by-layer growth. In particular, the synthesis of composites based on aluminum bronze and steel can be realized by wire-feed electron beam additive manufacturing. In order to implement composite materials produced via additive technologies in a humid (marine) climate, it is necessary to ensure not only high strength, but also corrosion properties. **The purpose of this work** is to study the corrosion resistance of composites, based on aluminum bronze *CuAl9Mn2* and stainless steel *ER 321* produced by dual-wire-feed electron beam additive manufacturing. **Research methods.** Examination of the surface of *CuAl9Mn2/ER 321* composites before and after corrosion tests was carried out by methods of voltammetry and electrochemical impedance spectroscopy using a potentiostat-galvanostat. **Results and discussion.** Using a complex of electrochemical methods, it is revealed that the developed composites with a volume fraction of steel ≥ 25 % demonstrate a significant decrease in anodic current densities and a simultaneous increase in charge transfer resistance. Composites with a steel content of 75 vol. % are characterized by the highest corrosion properties in 3.5 wt. % *NaCl* solution, which is referred to a reduction in corrosion rate by 9.5 times compared to aluminum bronze. It is shown that the main processes occurring on the surface of the composites (*CuAl9Mn2* + + *ER 321*) are anodic oxidation of copper and iron, leading to the formation of corrosion products – Cu_2O and $FeCl_2$.

For citation: Semin V.O., Panfilov A.O., Utyaganova V.R., Vorontsov A.V., Zykova A.P. Corrosion properties of CuAl9Mn2/ER 321 composites formed by dual-wire-feed electron beam additive manufacturing. *Obrabotka metallov (tekhnologiya, oborudovanie, instrumenty) = Metal Working and Material Science*, 2024, vol. 26, no. 3, pp. 163–178. DOI: 10.17212/1994-6309-2024-26.3-163-178. (In Russian).

Introduction

It is well known that aluminum bronzes are distinguished among copper alloys by its high mechanical, corrosion and anti-friction properties [1, 2]. These alloys are widely used in the marine industry (valves, fittings, ship propellers, pump shafts, valve rods, water chambers of heat exchangers etc.) [3]. Bronze alloyed with ~10 wt. % *Al*, exhibits the best comprehensive properties and is considered to be the most widely used materials in the aluminum bronze group of alloys. When *Al* content reaches a solubility limit (9.4 wt. %), the friction coefficient decreases, but a wear loss during wear on steel increases [4, 5]. The microstructure, corrosion resistance and wear resistance of aluminum bronze alloys are complex and

*** Corresponding author**
Zykova Anna P., Ph.D. (Physics and Mathematics), Head Laboratory
Institute of Strength Physics and Materials Sciences SB RAS,
2/4, pr. Akademicheskii,
634055, Tomsk, Russian Federation
Tel.: +7 3822 286866, **e-mail:** zykovaap@ispms.ru

significantly depend on the composition and cooling rate during the alloy production. Ordered structures, martensitic transformations and intermetallic compounds may form in this group of alloys [6–8]. Multiphase composition and microstructure of the copper alloys greatly affect both tribological and corrosion characteristics [3], therefore, increased attention is paid to studies of the microstructure and properties of these materials.

One of the high-tech and extensively developed methods for producing composite copper- and steel-based materials is additive technologies, which make it possible to fabricate complex parts through a layer-by-layer growth and have many advantages over traditional metallurgical technologies [1, 9–12].

In general, coatings or bimetallic alloys composed of aluminum bronze and steel are studied [10–12]. For example, in the paper [1], the tribocorrosion properties of additively produced stainless steel *316* (*316SS*), impregnated with bronze in seawater were studied. Tribological test showed that the resulting composite had yield strength and friction characteristics comparable to the conventional *316SS* steel, while significant improvement in wear resistance was achieved at the test loads up to 80 N and reciprocating frequencies up to 20 Hz. It is assumed that the bronze smeared along the wear track serves as a solid lubricant, so the resulting passive oxide film seems to be a tribofilm that inhibits an abrasive wear at high loads. At the same time, an assessing the corrosion properties of various types of bronzes [1, 2] do not allow to unambiguously conclude about the nature of the corrosion damage, as well as the mechanisms of formation of corrosion products (CuO, Cu_2O, etc.) in copper alloys during immersion into chloride-containing solutions.

To date, the fabrication of composites based on aluminum bronze and steel could be performed using modern metallurgical methods of additive manufacturing, for example, electron beam melting. In particular, this technology is realized using a dual-wire-feed electron beam additive manufacturing (*EBAM*) method [13–15]. Earlier, the authors of this work produced composites based on aluminum bronze (*CuAl9Mn2*) and stainless steel (*ER 321*) using *EBAM* [13, 16]. It was found that depending on the "*CuAl9Mn2* : *ER 321*" ratio the structural-phase states of the obtained composites were different and its mechanical characteristics could be improved. Our ongoing study aims to reveal the operating characteristics of the "*CuAl9Mn2*/*ER 321*" composites. The kinetics of a charge transfer at the interfaces and the factors responsible for the resistance to the appearance of the corrosive currents between microgalvanic elements (copper- and iron-based phases) remain poorly studied issues.

The purpose of the work is to study the corrosion resistance of the composites based on *CuAl9Mn2* aluminum bronze and *ER 321* stainless steel, produced by a dual-wire-feed electron beam additive manufacturing. The scientific objectives of this study include (i) a comprehensive assessment of the electrochemical behavior of *CuAl9Mn2*/*ER 321* composites in marine solution (3.5 wt. % *NaCl*); (ii) a determination of the phase composition of corrosion products and type of corrosion damage; (iii) an identification of the predominant corrosion mechanism.

Methodology

In order to fabricate composites, the wires ∅1.6 mm of *CuAl9Mn2* aluminum bronze and *ER 321* stainless steel were used as raw materials. A stainless steel plate with a thickness of 10 mm was chosen as a substrate. To produce the bronze-steel composites, an *EBAM* installation, equipped with two wire feeders, was used (Fig. 1). The following parameters of the *EBAM* process were used: beam accelerating voltage 30 kV, beam current from 44 to 77 mA, print speed (movement of the working stage) was 400 mm/min. The required volume ratio of bronze and steel was maintained constant during processing by automatically adjusting the appropriate ratio of the wire feed speeds. As a result, the composites with a size of 80×120×8 mm^3 and a volume ratio *CuAl9Mn2* : *ER 321* = 90 : 10, 75 : 25, 50 : 50 and 25 : 75 were obtained. A more detailed method for producing composites is presented in early works [13, 16].

For metallographic studies, the specimens were cut out by means of an electrical discharge machine, according to the Fig. 1. Then, the specimens were subjected to mechanical polishing using an abrasive sandpaper, followed by polishing with a diamond paste. To assess the mechanical properties, the specimens were tested for uniaxial static tension, and the microhardness was measured by the *Vickers* method [13, 16].

The studies of the electrochemical (corrosion) properties of the specimens were carried out by voltammetry and electrochemical impedance spectroscopy (*EIS*) using a potentiostat-galvanostat *PalmSens 4*. The electrochemical cell was a three-electrode system in which the specimen under study served as the working electrode. A silver chloride electrode filled with 1 M *KCl* was used as a reference electrode. The auxiliary electrode was a graphite electrode. In the method of a linear polarization, the following parameters were set: potential range varied from –0.5 to 0 V, scan rate was 1 mV/s. In the cyclic voltammetry (*CV*) method, the scan rate was 20 V/s, and the potential varied from –1.2 V to +1.2 V. Using the electrochemical impedance spectroscopy (*EIS*) method, the electrochemical processes associated with a charge (ions, electrons) transfer and diffusion of charges in the electrical double layer were identified. Processing of *EIS* results was carried out by modeling equivalent electrical circuits that describe the impedance behavior of the "electrolyte/composite" system. For impedance measurements, the *DC* voltage ($\boldsymbol{E_{dc}}$) was set equal to the open circuit potential. The amplitude of the sinusoidal signal ($\boldsymbol{E_{ac}}$) was 0.01 V. The frequency range was varied from 0.1 to 10^5 Hz. All measurements were performed at 3.5 wt. % *NaCl*. *Pearson's* criterion (χ^2), used to fit the raw data, ranged from 10^{-3} to 10^{-4}, and the fitting errors did not exceed 10 %.

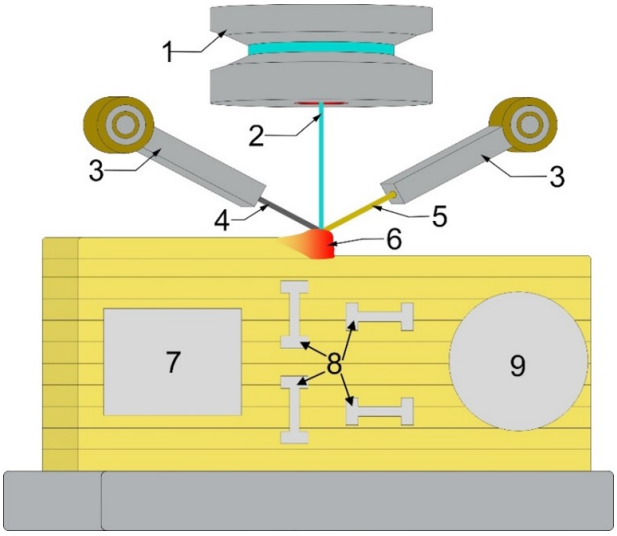

Fig. 1. Scheme of *EBAM* process for composites and test specimens cut-up sketch:

1 – electron beam gun; 2 – electron beam; 3 – wire feeders; 4 – *ER 321* wire; 5 – *CuAl9Mn2* wire; 6 – melt pool; 7 – specimen for structural studies; 8 – specimens for tensile test; 9 – specimen for corrosion testing

PSTrace 5.8 software was used to calculate corrosion parameters. Quantitative assessment of the polarization resistance ($\boldsymbol{R_p}$) of the composites was done by the *Stern-Geary* equation:

$$R_p = (\beta_a \beta_c)/(2.303 i_{corr}(\beta_a + \beta_c)),$$

where $\boldsymbol{\beta_a}$ is the slope of the anodic branch; $\boldsymbol{\beta_c}$ is the slope of the cathodic branch; $\boldsymbol{i_{corr}}$ is the corrosion current density.

The surface morphology of the specimens after *CV* measurements was analyzed using a *LEO EVO 50* scanning electron microscope (*Zeiss*, Germany) equipped with an energy dispersive spectrometer *INCA Energy* (*Oxford instruments*, UK).

Results and Discussion

Structural-phase state and mechanical characteristics of the CuAl9Mn2/ER 321 composites

Previously, the authors found out the features, associated with formation of the structural-phase states in the aluminum bronze, stainless steel and *CuAl9Mn2*/*ER 321* composites obtained by the *EBAM* method. It has been observed that aluminum bronze produced by the *EBAM* method is characterized by a columnar dendritic structure [8]. The martensitic β′ phase is located along the boundaries of the α-*Cu* grains (Fig. 2, *a*). The microstructure of the additively manufactured stainless steel *ER 321* is characterized by elongated austenite grains exhibiting long and straight dendritic colonies (Fig. 2, *b*) [17]. Along the grain boundaries of the γ-*Fe* phase the δ-*Fe* phase is revealed (Fig. 2, *b*).

When the volume ratio *CuAl9Mn2* : *ER 321* of the composite is 90:10, the structure of the composite, in comparison with the aluminum bronze, possesses a smaller size of the **α**-*Cu* grains, while the volume fraction of the β′ phase decreases significantly. Also, a precipitation of the globular **α**-*Fe*(*Cr*) particles and dispersed particles of the $\boldsymbol{\kappa_{iv}}$-phase (Fe_3Al) are observed (Fig. 2, *c*) [13]. The α-*Cu* solid solution contains

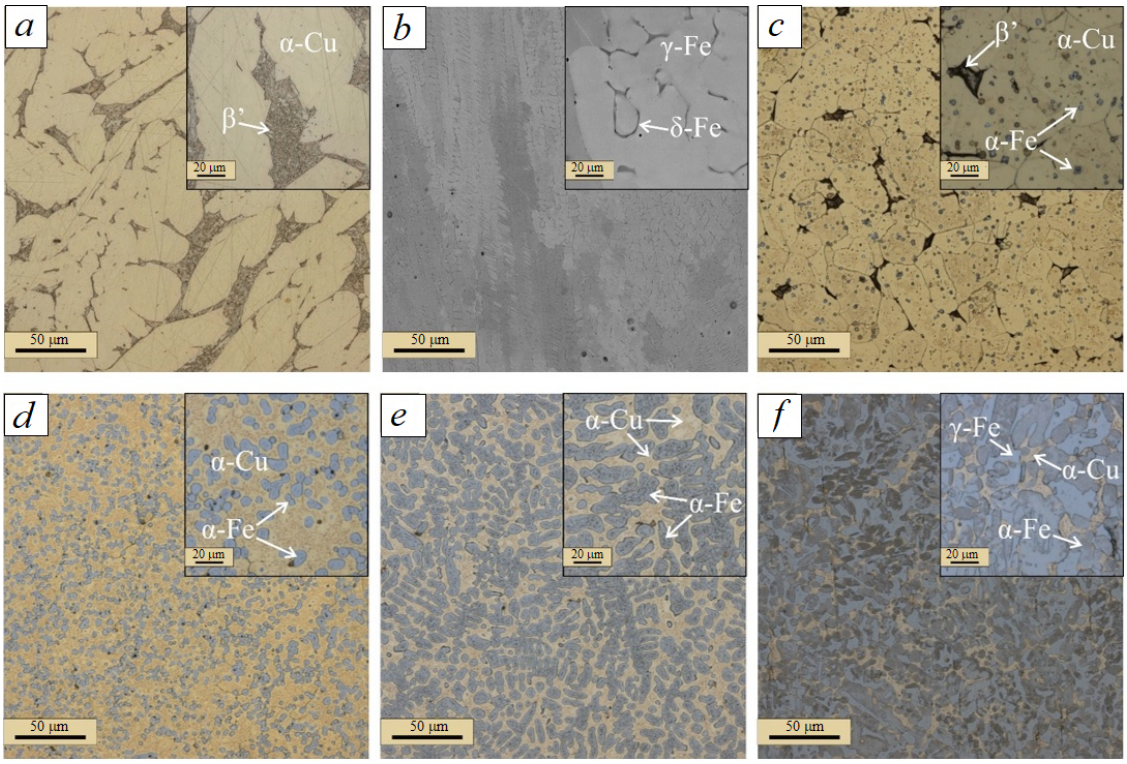

Fig. 2. Microstructure of *CuAl9Mn2* (*a*), *ER 321* (*b*) and composites with a ratio of *CuAl9Mn2* : *SS321* = 90 : 10 (*c*), 25 : 75 (*d*), 50 : 50 (*e*) and 25 : 75 (*f*)

~1 at. % *Ni*. Increasing the concentration of steel *ER 321* to 25 and 50 vol. %, leads to complete suppression of the **β′**-phase, **α**-*Fe*(*Cr*) grains are formed, within which fine particles with a **β′**/*AlNi* core/shell structure are observed (Fig. 2, *d*, *e*). In this case, in the **α**-*Fe*(*Cr*) solid solution, the precipitation of the dispersed particles of the $\boldsymbol{\kappa}_{iv}$-phase is observed, the average size of which increases with increasing concentration of steel in aluminum bronze [13].

If the ratio *CuAl9Mn2* : *ER 321* reaches 25 : 75, a three-phase structure is formed, consisting of 44 vol. % of **γ**-*Fe* phase, 32 vol. % of the **α**-*Fe* phase and 24 vol. % of the **α**-*Cu* phase (Fig. 2, *f*). Non-equilibrium cooling conditions lead to the precipitation of the dispersed secondary particles of copper and *NiAl* in the **γ**-*Fe* and **α**-*Fe* grains, respectively [16].

Static tensile tests have shown that yield strength and an ultimate strength for *CuAl9Mn2* and *ER 321* are 148 and 440 MPa, and 300 and 610 MPa, respectively (Table 1). A composite produced using a volume ratio *CuAl9Mn2* : *ER 321* = 90 : 10 shows the values of the yield strength and ultimate strength that are comparable to the steel, but much greater than those of the aluminum bronze (Table 1). Addition of the stainless steel up to 50 vol. % into the aluminum bronze during *EBAM* processing leads to the higher values of the yield strength and tensile strength than those of the *CuAl9Mn2* and *ER 321* (Table 1). At the same time, in the composite with the ratio *CuAl9Mn2* : *ER 321* = 25 : 75, a decrease in the yield strength and strength is observed by 240 and 160 MPa, respectively, compared to the composite *CuAl9Mn2* : *ER 321* = 50 : 50. However, the *ER 321* steel, diluted with aluminum bronze, shows improved mechanical characteristics compared to the pure *ER 321* steel (Table 1), that are similar to the properties of the composites based on *316SS* and tin bronze [1]. The microhardness of the *CuAl9Mn2*/*ER 321* composites increases from 1.4 GPa to 2.33 GPa when the volume fraction of the stainless steel increases up to 50 vol. %. In the case of the *CuAl9Mn2*/*ER 321* composites exhibiting a volume fraction 25:75, the microhardness decreases to 2.16 GPa (Table 1).

Assessment of the corrosion properties of the composites by means of voltamperometric methods

Fig. 3 shows cyclic voltammograms (*CVs*) demonstrating reversible redox reactions and irreversible anodic processes occurring on the surface of the working electrodes. Anodic oxidation of the metals

Table 1

Mechanical properties obtained by microhardness measuring and static uniaxial tensile tests

Specimen	Mechanical characteristics			
	$\sigma_{0.2}$, MPa	σ_u, MPa	ε, %	HV, GPa
CuAl9Mn2	148±25	440±101	62	1.4 ± 0.17
ER 321	300±42	610±136	35	1.63 ± 0.09
CuAl9Mn2 – 10% *ER 321*	296±43	640±145	28	1.46 ± 0.19
CuAl9Mn2 – 25% *ER 321*	321±49	635±130	25	1.75 ± 0.09
CuAl9Mn2 – 50% *ER 321*	610±97	813±183	12	2.33 ± 0.1
CuAl9Mn2 – 75% *ER 321*	370±55	652±145	33	2.16 ± 0.12

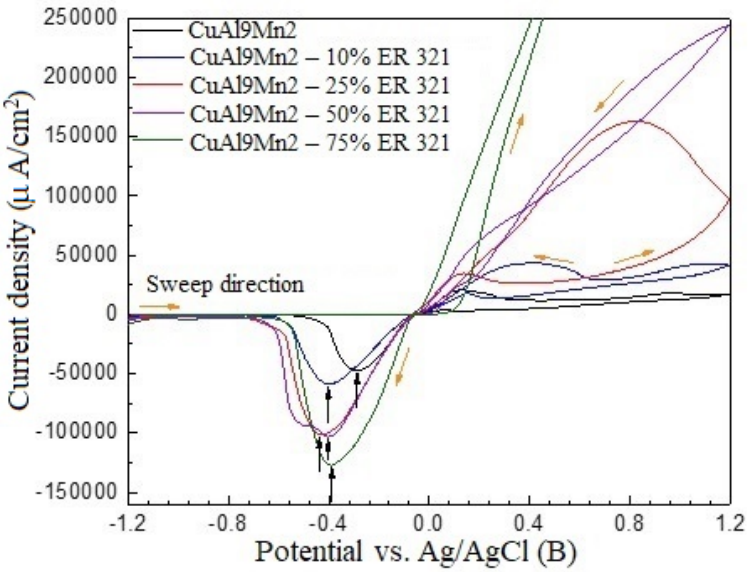

Fig. 3. Cyclic voltammograms (20 mV/s) of specimens obtained in 3.5 wt. % *NaCl* solution. The black arrows indicate peaks of the current density in the cathode branch corresponding to the copper reduction reaction

(*Fe*, *Cu*, *Al*) is observed at electric potentials that are beyond the passive state region (from $\boldsymbol{E_1}$ = –1.20 V to $\boldsymbol{E_2}$ = –0.05 V). In the positive region of the potentials (from +0.0 V to +1.2 V), all specimens, including *CuAl9Mn2*, exhibit a sharp increase in the current density due to the following (possible) anodic processes [18, 19]:

$$Al \rightarrow Al^{3+} + 3e^- \quad (1)$$

$$Al^{3+} + 3OH^- \rightarrow Al(OH)_3 \quad (2)$$

$$Cu \rightarrow Cu^+ + e^-,\ Cu^+ \rightarrow Cu^{2+} + e^- \quad (3)$$

$$Cu + Cl^- \rightarrow CuCl + e^-,\ 2CuCl + H_2O \rightarrow Cu_2O + 2H^+ + 2Cl^- \quad (4)$$

$$CuCl + Cl^- \rightarrow CuCl_2^- \rightarrow Cu^{2+} + 2Cl^- + e^- \quad (5)$$

$$2Cu^+ + H_2O \rightarrow Cu_2O + 2H^+ \quad (6)$$

$$Fe \rightarrow Fe^{2+} + 2e^{-},\ Fe - 2e^{-} + 2H_2O \rightarrow Fe(OH)_2 + 2H^{+} \quad (7)$$

$$Fe^{2+} + 2Cl^{-} \rightarrow FeCl_2 \quad (8)$$

In the cathodic branch of the *CV* curves, corresponding to the region from +0.05 V to –0.80 V, the peaks of copper reduction are seen (marked by black arrows in Fig. 3), which are shifted relative to each for the specimens having different volume fractions of the steel. In the *CuAl9Mn2* specimen, the cathodic reduction of copper ($Cu^{2+} + 2e^{-} \rightarrow Cu$) occurs at the highest potential $\boldsymbol{E}$ = –0.29 V (relative to *Ag*/*AgCl*). In turn, in the *CuAl9Mn2* + 50 vol. % *ER 321* specimen the same reaction takes place at the lowest potential ($\boldsymbol{E}$ = –0.51 V). During reiteration of the *CV* measurements the same peaks of oxidation and reduction of copper are observed, which indicates the reversible nature of the reaction $Cu \rightleftarrows Cu^{2+} + 2e^{-}$. In addition, the following cathodic processes are expected to occur in aqueous solutions, in which the **α**-*Cu* phase will act as a reducing agent:

$$O_2 + 4e^{-} + 2H_2O \rightarrow 4OH^{-} \quad (9)$$

$$O_2 + 4H^{+} + 4e^{-} \rightarrow 4OH^{-} \quad (10)$$

$$2H_2O + 2e^{-} \rightarrow H_2 + 2OH^{-} \quad (11)$$

$$2H^{+} + 2e^{-} \rightarrow H_2 \quad (12)$$

In the specimens containing from 50 to 75 vol. % of the *ER 321* steel, the electrochemically active components of the composite are **γ**-*Fe*, **α**-*Fe* and **α**-*Cu* phases. It is reasonable to assume that in the 3.5 wt. % *NaCl* solution the reactions, associated with the formation of *Fe*/*Cu* galvanic couples, initiate. In the presence of strong oxidizing agents (Cl^{-}), both metals (*Fe*, *Cu*) in these phases may oxidize. In this case, the electrons released in the reactions (3) and (7) would be captured by copper, which acts as a cathode in the *Fe*/*Cu* galvanic couple due to the significant difference in the standard reduction potentials ($\boldsymbol{E}_{Cu(2+)/Cu}$ = + 0.34 V, $\boldsymbol{E}_{Fe(2+)/Fe}$ = –0.44 V). Based on analysis of the *CV* curves it follows that the main processes on the surface of the composites (*CuAl9Mn2* + *ER 321*) are anodic oxidation of copper and iron, formation of chlorides ($FeCl_2$, $CuCl_2$), discharge of the oxidizing agent (oxygen) and reduction of copper (reversible reaction).

The corrosion rate of the specimens was assessed using a linear potential scan. In contrast to *CV* curves (Fig. 3), only irreversible anodic processes are observed in the polarization curves (Fig. 4), leading to the appearance of corrosion damage onto the surface of the working electrodes. All specimens are characterized

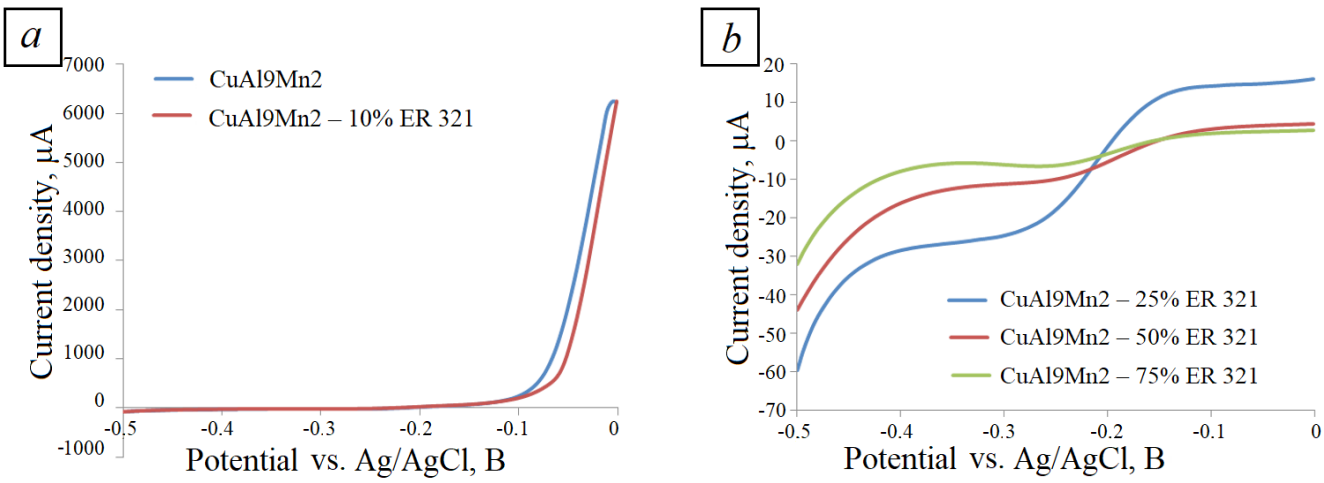

Fig. 4. Voltammograms obtained in 3.5 wt. % *NaCl* solution for *CuAl9Mn2* and composites exhibiting 10 vol. % (*a*) and 25, 50, 75 vol. % *ER 321* (*b*)

by the presence of a passive state region, limited by a narrower potential window: from –0.3 V to –0.1 V for the initial bronze and *CuAl9Mn2* + 10 vol. % *ER 321* (Fig. 4, *a*); from –0.4 V to –0.2 V for composites containing 25, 50 and 75 vol. % *ER 321* (Fig. 4, *b*). A sharp increase in anodic currents is accompanied by an intense dissolution of the outer surface layer at $\boldsymbol{E}$ = –0.1 V. It is important to note that composites with a larger volume fraction of steel (≥ 25 %) demonstrate lower values of the anodic currents (Fig. 4, *b*), which indicates a formation of a protective oxide film with apparent dielectric properties onto the surface of the composites.

Fig. 5 shows the voltammetric dependences, plotted in logarithmic coordinates, of the same specimens in 3.5 wt. % *NaCl* solution. Extrapolation of these curves by the *Tafel* function, which takes into account the slopes of the cathodic ($\boldsymbol{b}_c$) and anodic ($\boldsymbol{b}_a$) branches, allows to calculate the corrosion current densities and polarization resistance ($\boldsymbol{R}_p$) using the *Stern-Geary* equation [20]. The corrosion parameters are given in Table 2. Two important conclusions could be made from the analysis of the *Tafel* curves. With an increase in steel content in the composites, the corrosion potential ($\boldsymbol{E}_{cor}$, Table 2) shifts to the region of the positive potentials. This is, most likely, due to the fact that the surface of the samples is passivated not by copper oxides, but by nickel and chromium oxides. This suggestion is supported by the lower standard reduction potential of *Ni* and *Cr* ($\boldsymbol{E}_{Cr(3+)/Cr}$ = –0.744 V, $\boldsymbol{E}_{Ni(2+)/Ni}$ = –0.257 V) than that of copper ($\boldsymbol{E}_{Cu(2+)/Cu}$ = +0.34 V). The densities of corrosion currents naturally decrease from 11.010 to 0.512 μA/cm^2 for the composites obtained at the ratios *CuAl9Mn2* : *ER 321* = 90 : 10; 25 : 75; 50 : 50 and 25 : 75, and the polarization resistance, on the contrary, increases by almost an order of magnitude (Table 2). It can be concluded that the formation of the austenitic **γ**-*Fe* phase in the surface layer of the samples with a volume fraction of steel ≥ 50 % more effectively prevents the development of corrosion processes than alloying the **α**-*Cu* phase with nickel and chromium. Thus, using the *EBAM* method, the composites characterized by a lower (~9.5 times) corrosion rate in the marine environment could be fabricated.

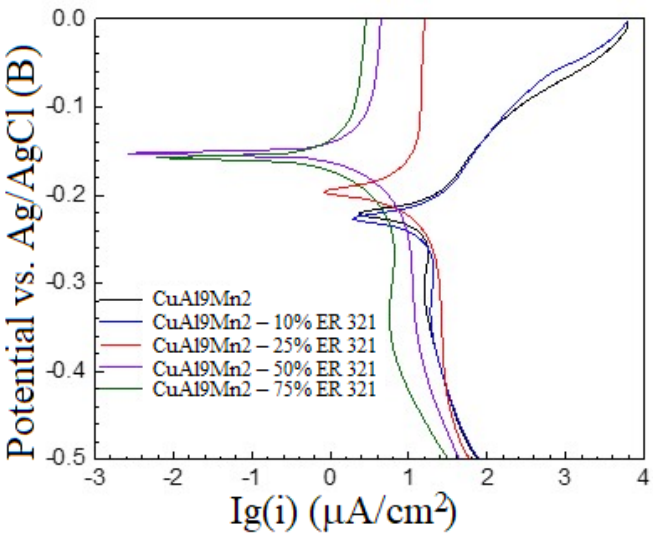

Fig. 5. Potentiodynamic polarization curves obtained in the same electrolyte (3.5 wt. % *NaCl* solution) for the *CuAl9Mn2* and composites

EIS study of the electrochemical behavior of the specimens

In order to reveal the electrochemical properties of the *CuAl9Mn2*/*ER 321* composites, the impedance spectra were obtained relative to the open-circuit potential and plotted in *Nyquist* coordinates before and

Table 2

Corrosion parameters determined from polarization curves by *Tafel* extrapolation of the *CuAl9Mn2* and composites

Sample	Corrosion parameters				
	E_{cor}, V	I_{cor}, μA/cm^2	β_a, V	β_c, V	R_p, Ohm·cm^2
CuAl9Mn2	–0.207	11.390	0.066	0.287	2,048
CuAl9Mn2 – 10% ER 321	–0.218	11.010	0.071	0.209	2,091
CuAl9Mn2 – 25% ER 321	–0.194	4.945	0.125	0.098	4,810
CuAl9Mn2 – 50% ER 321	–0.147	1.043	0.125	0.098	16,300
CuAl9Mn2 – 75% ER 321	–0.149	0.512	0.039	0.061	20,100

after potentiodynamic polarization tests (Fig. 6). The dots in the diagrams indicate the experimental values of the impedance (real and imaginary parts), and the solid lines indicate the approximation by the model – an equivalent electrical circuit (Fig. 6, *f*).

It is important to note that in a corrosive media (3.5 wt. % *NaCl*) the electrochemical activity of the composites, promoting anodic reactions, is regulated by the ratio *CuAl9Mn2* : *ER 321*. Indeed, the impedance of the initial bronze specimens (Fig. 6, *a*) before corrosion tests is described by a relatively simple equivalent circuit, including a constant phase element ($\boldsymbol{Q_1}$), solution resistance ($\boldsymbol{R_s}$) and charge transfer ($\boldsymbol{R_{ct}}$) and *Warburg* element (***W***). The fitted *EIS* data are given in Table 3. From the Table 3 it follows that the *CuAl9Mn2* specimen shows high electrochemical activity because of the low charge transfer resistance (Fig. 3, *a*; Table 3). The presence of a *Warburg* element indicates the diffusion of charges (e^-, Cu^+, Cu^{2+}, Fe^{2+}) through the electrical double layer into the solution. It is interesting to emphasize that after corrosion tests the $\boldsymbol{R_{ct}}$ value decreases by ~4.3 times. This observation can be explained by the fact that anodic processes (oxidation of copper to Cu^{2+}) initiate the dissolution of the natural oxide film and repassivation of the surface, which leads to a change in the kinetics of a charge transfer in the electric double layer (Fig. 6, *a*; Table 3).

For the composite fabricated at the ratio *CuAl9Mn2* : *ER 321* = 90 : 10 (Fig. 6, *b*), the equivalent circuit remains the same, and the $\boldsymbol{R_{ct}}$ value decreases by ~3 times (Table 3) due to repassivation of the surface

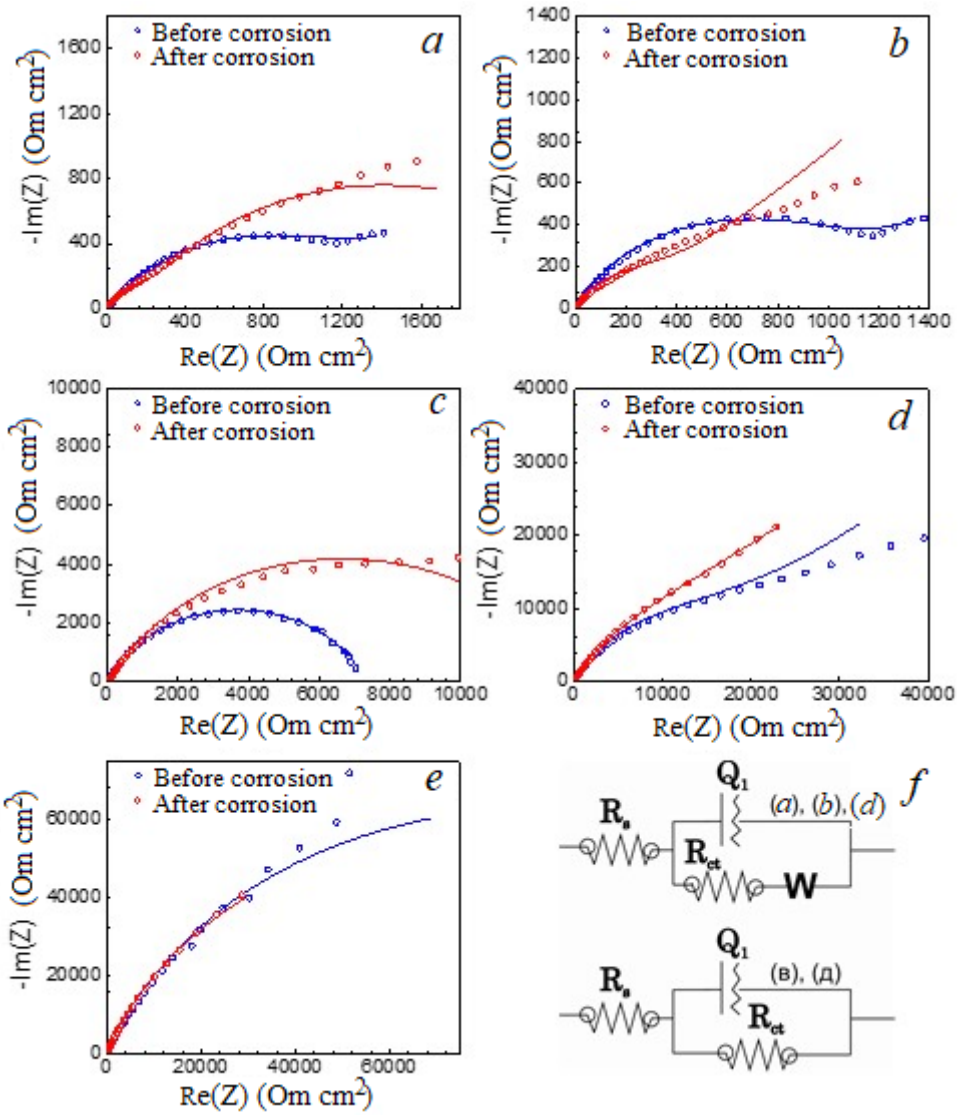

Fig. 6. Nyquist plots of *CuAl9Mn2* (*a*) and composites with a ratio of *CuAl9Mn2* : *ER 321* = 90 : 10 (*b*); 25 : 75 (*c*); 50 : 50 (*d*); 25 : 75 (*e*) and equivalent electrical circuits (*f*)

Table 3

Parameters of equivalent electrical circuits for *CuAl9Mn2* and *CuAl9Mn2*/*ER 321* composites before and after potentiodynamic polarization

Before corrosion					
Element of the electrical circuit	*CuAl9Mn2*	*CuAl9Mn2* : *ER 321*			
		90 : 10	75 : 25	50 : 50	25 : 75
Solution resistance, Ohm·cm^2	5	5	70	4	67
Charge transfer resistance, Ohm·cm^2	1,385	1,158	7,269	21,630	177,000
Warburg element, kOhm/c$^{-0.5}$	0.21	0.26	–	15.75	–
After corrosion					
Solution resistance, Ohm·cm^2	5	4.9	69	43	71
Charge transfer resistance, Ohm·cm^2	324	396	13,210	25,510	154,200
Warburg element, kOhm/c$^{-0.5}$	1.05	0.64	–	16.50	–

layer. With an increase in the share of steel in the composite up to 25 vol. % the *Nyquist* diagram is a semicircle without a linear part in the low frequency region, therefore the equivalent circuit does not include the *Warburg* element responsible for the charge diffusion. The $\boldsymbol{R}_{\mathbf{ct}}$ value increases from 7,269 to 13,210 Ohm·cm^2 (Fig. 6, *c*, Table 3) after a potentiodynamic polarization test, which indicates a higher passivation ability of this composite in comparison with the sample having 10 vol. % of the *ER 321* steel. A composite with the ratio *CuAl9Mn2* : *ER 321* = 50 : 50 has a quite high charge transfer resistance before and after corrosion tests (Table 3). The presence of a semicircle in the *Nyquist* diagram (Fig. 6, *d*) and a linear dependence, when both real and imaginary parts > 10,000 Ohm·cm^2, indicate oxidation of the material and the release (diffusion) of the charged particles into solution.

In the impedance spectra of the composite with the ratio *CuAl9Mn2* : *ER 321* = 25 : 75, only a part of the semicircle is present (Fig. 6, *e*), which indicates a significant charge transfer resistance $\boldsymbol{R}_{\mathbf{ct}}$ (~177,000 Ohm·cm^2). At the same time, an electrical discharge of the double layer does not occur and diffusion of charges into the solution is not occurred (Fig. 6, *c*, Table 3). As can be seen from Table 3, the charge transfer resistance of this specimen decreases slightly after corrosion. In this case, the anodic oxidation of iron and copper will be hindered if a repassivation of the surface layer takes place after appearance of the corrosion damage. We conclude that the least electrochemically active specimen is the composite with the ratio *CuAl9Mn2* : *ER 321* = 25 : 75, since it is characterized by the maximum value of $\boldsymbol{R}_{\mathbf{ct}}$, which, in turn, is inversely proportional to the density of corrosion current. Summarizing the data of electrochemical experiments (*EIS*, *CV*, linear polarization), we conclude that the composite with 75 vol. % of the steel could be considered to be the most corrosion resistant one. The lowest corrosion resistance was found for the *CuAl9Mn2* and the composite with 10 vol. % of the *ER 321* steel.

Based on electrochemical reactions (1)–(12) and literature data on the corrosion properties of *Fe-Cu* alloys [21] and bronze [22, 23], we can expect that the possible corrosion products of the studied *CuAl9Mn2*/*ER 321* composites are insoluble or poorly soluble compounds – copper and iron oxides. In the X-ray diffraction patterns of the *CuAl9Mn2* (Fig. 7, *a*) and the composite *CuAl9Mn2* – 10 vol. % *ER 321* (Fig. 7, *b*), subjected to corrosion tests in the cyclic potential sweep mode, the main diffraction lines from the matrix phases are recorded (**α**-*Cu*, **β′**, **α**-(*Fe*,*Cr*), Cu_3Al), found earlier in [13]. In this case, additional reflections belonging to the Cu_2O and $FeCl_2$ phases are detected (Fig. 7, *a, b*). These phases (Cu_2O, $FeCl_2$) can be formed as a result of microgalvanic corrosion occurring primarily at the grain boundaries between **α**-(*Fe*,*Cr*) ferrite particles and the **α**-*Cu* matrix in chloride-containing electrolytes.

Analysis of the corrosion damage (Fig. 7, *c*, *d*) on the composite's surface has shown that the mechanisms of localized corrosion are realized in the *CuAl9Mn2* alloy, leading to the appearance of shallow pits

and selective dissolution of copper phases. The dissolution of copper according to reactions (3)–(6) is limited by a protective oxide film, which impedes the spread of corrosion pits over the entire surface. Therefore, the morphology of the *CuAl9Mn2* alloy after *CV* measurements is characterized by protrusions ("flakes") and neighboring areas free of corrosion pits (Fig. 7, *c*). On the contrary, in the specimen *CuAl9Mn2* – 10 vol. % *ER 312* an intensive corrosion damage (Fig. 7, *d*) of a pitting nature is observed. Numerous and deeper pits predominate, forming a network of porous structures. In our opinion, the nature of corrosion damage in the *CuAl9Mn2*/*ER 312* composites is associated with contact and crevice corrosion. When the **α**-*Cu* and **α**-(*Fe*,*Cr*) phases come into contact, the *Fe*/*Cu* galvanic couples are formed, which change the kinetics of the redox reactions due to the movement of charges between dissimilar metals (*Fe*, *Cu*) with different electrochemical potentials. As a result of contact corrosion, the primary sites for pitting initiation are the **α**-*Cu*/**α**-(*Fe*,*Cr*) interphase boundaries due to the formation of corrosion couples (Fig. 7, *e*). In this case, the working surface of the *CuAl9Mn2* – 10 vol. % *ER 321* composite is divided into cathodic (matrix grains **α**-*Cu*) and anodic (particles **α**-(*Fe*,*Cr*)) areas.

It is important to note that due to a spontaneous passivation of the ferrite phase (presumably by nickel and chromium oxides), its dissolution in 3.5 wt. % *NaCl* solution is limited, while *Cu*-containing phases are

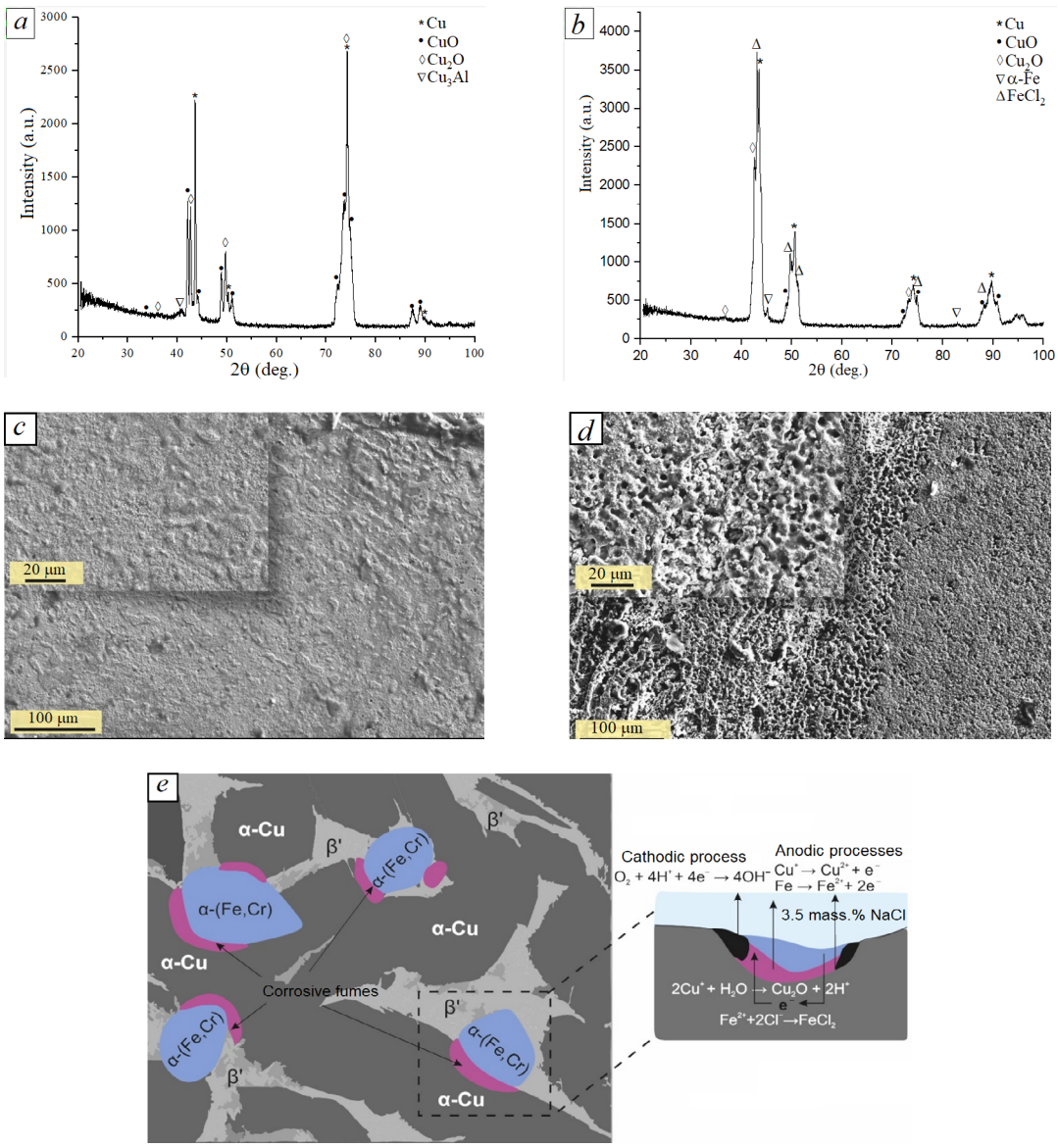

Fig. 7. XRD patterns and *SEM* images of the surface after corrosion tests of *CuAl9Mn2* (*a*, *c*) and composite *CuAl9Mn2* – 10% *ER 321* (*b*, *d*); *e* – scheme of the formation of pitting damage on the composite surface due to galvanic corrosion

subject to continuous anodic oxidation accompanied by the formation of Cu^{+} and Cu^{2+} ions. Additionally, cathodic processes described by reactions (9), (10) are possible on the surface of copper phases, partially impeding its ionization. Thus, in the presence of strong oxidizing agents (Cl^{-}) the formation of corrosion pits in the composites based on aluminum bronze and stainless steel will be accelerated if the formation of *Fe*/*Cr* microgalvanic couples is not prevented (Fig. 7, *e*). In order to increase the corrosion properties of these composites, it is necessary to carry out surface treatments leading to the formation of continuous and dielectric oxide films on the surface of **α**-*Cu*, **α**-(*Fe*,*Cr*) and **γ**-(*Fe*,*Ni*,*Cr*) phases, preventing a direct electrochemical contact of *Fe*/*Cr* at interphase boundaries.

Conclusions

The paper presents experimental results of the electrochemical behavior of the *CuAl9Mn2*/*ER 321* composites obtained by the additive electron beam method. With an increase in the volume fraction of steel in aluminum bronze, the microhardness, yield strength and strength of the composites change in a non-monotonic manner and reach the highest values in the specimen containing 50 vol. % of the steel. Corrosion resistance of the specimens in 3.5 wt. % *NaCl* solution was estimated using the *Tafel* extrapolation method. It has been found that the densities of corrosion currents monotonically decrease for the composites obtained at the ratios *CuAl9Mn2* : *ER 321* = 90 : 10, 75 : 25, 50 : 50 and 25 : 75, and the polarization resistance, that is inversely proportional to the corrosion rate, increases by an order of magnitude. A comprehensive assessment of the electrochemical properties of the specimens using impedance spectroscopy and cyclic voltammetry has shown that the most corrosion resistant is a composite with 75 vol. % of the *ER 321* steel, and the lowest corrosion resistance is demonstrated by the *CuAl9Mn2* alloy and a composite with 10 vol. % of the ER 321 steel. It has been observed that the main processes on the surface of composites are anodic oxidation of *Cu* and *Fe*, leading to the formation of corrosion products – Cu_2O and $FeCl_2$. It is assumed that the main mechanism of the corrosion damage in the *CuAl9Mn2*/*ER 321* composites is a galvanic corrosion caused by the formation of galvanic *Fe*/*Cr* pairs at the interphase boundaries between ferrite particles **α**-(*Fe*,*Cr*) and the **α**-*Cu* matrix.

References

1. Wang L., Tieu A.K., Lu S., Jamali S., Hai G., Zhu Q., Nguyen H.H., Cui S. Sliding wear behavior and electrochemical properties of binder jet additively manufactured 316SS /bronze composites in marine environment. *Tribology International*, 2021, vol. 156, p. 106810. DOI: 10.1016/j.triboint.2020.106810.

2. Ateya B.G., Ashour E.A., Sayed S.M. Corrosion of α-Al bronze in saline water. *Journal of the Electrochemical Society*, 1994, vol. 141 (1), p. 71. DOI: 10.1149/1.2054712.

3. Davis J.R., ed. *Copper and copper alloys*. Materials Park, OH, ASM International, 2001. 869 p.

4. Blau P.J. Investigation of the nature of micro-indentation hardness gradients below sliding contacts in five copper alloys worn against 52100 steel. *Journal of Materials Science*, 1984, vol. 19, pp. 1957–1968. DOI: 10.1007/BF00550266.

5. Shi Z., Sun Y., Bloyce A., Bell T. Unlubricated rolling-sliding wear mechanisms of complex aluminium bronze against steel. *Wear*, 1996, vol. 193 (2), pp. 235–241. DOI: 10.1016/0043-1648(95)06773-6.

6. Kwarciak J., Bojarski Z., Morawiec H. Phase transformation in martensite of Cu-12.4% Al. *Journal of Materials Science*, 1986, vol. 21, pp. 788–792. DOI: 10.1007/BF01117355.

7. Adorno A.T., Guerreiro M.R., Benedetti A.V. Isothermal aging kinetics in the Cu–19 at.%Al alloy. *Journal of Alloys and Compounds*, 2001, vol. 315 (1–2), pp. 150–157. DOI: 10.1016/S0925-8388(00)01268-8.

8. Zykova A.P., Panfilov A.O., Chumaevskii A.V., Vorontsov A.V., Nikonov S.Yu., Moskvichev E.N., Gurianov D.A., Savchenko N.L., Tarasov S.Yu., Kolubaev E.A. Formation of microstructure and mechanical characteristics in electron beam additive manufacturing of aluminum bronze with an in-situ adjustment of the heat input. *Russian Physics Journal*, 2022, vol. 65, pp. 811–817. DOI: 10.1007/s11182-022-02701-6.

9. Li W.S., Wang Z.P., Lu Y., Gao Y., Xu J.L. Preparation, mechanical properties and wear behaviours of novel aluminum bronze for dies. *Transactions of Nonferrous Metals Society of China*, 2006, vol. 16 (3), pp. 607–612. DOI: 10.1016/S1003-6326(06)60107-6.

10. Dharmendra C., Shakerin S., Janaki Ram G.D., Mohammadi M. Wire-arc additive manufacturing of nickel aluminum bronze/stainless steel hybrid parts – Interfacial characterization, prospects, and problems. *Materialia*, 2020, vol. 13, p. 100834. DOI: 10.1016/j.mtla.2020.100834.

11. Dong L., Chen W., Hou L., Liu Y., Luo Q. Metallurgical process analysis and microstructure characterization of the bonding interface of QAl9-4 aluminum bronze and 304 stainless steel composite materials. *Journal of Materials Processing Technology*, 2016, vol. 238, pp. 325–332. DOI: 10.1016/j.jmatprotec.2016.07.041.

12. Makarenko K., Dubinin O., Shornikov P., Shishkovsky I. Specific aspects of the transitional layer forming in the aluminium bronze – stainless steel functionally graded structures after laser metal deposition. *Procedia CIRP*, 2020, vol. 94, pp. 346–351. DOI: 10.1016/j.procir.2020.09.143.

13. Zykova A., Panfilov A., Chumaevskii A., Vorontsov A., Moskvichev E., Nikonov S., Gurianov D., Savchenko N., Kolubaev E., Tarasov S. In-situ dispersion hardened aluminum bronze/steel composites prepared using a double wire electron beam additive manufacturing. *Progress in Additive Manufacturing*, 2023, vol. 8, pp. 1067–1082. DOI: 10.1007/s40964-022-00378-4.

14. Zykova A., Nikolaeva A., Panfilov A., Vorontsov A., Nikonenko A., Dobrovolsky A., Chumaevskii A., Gurianov D., Filippov A., Semenchuk N., Savchenko N., Kolubaev E., Tarasov S. Microstructures and phases in electron beam additively manufactured Ti-Al-Mo-Zr-V/CuAl9Mn2 alloy. *Materials*, 2023, vol. 16 (12), p. 4279. DOI: 10.3390/ma16124279.

15. Zykova A., Chumaevskii A., Panfilov A., Vorontsov A., Nikolaeva A., Osipovich K., Gusarova A., Chebodaeva V., Nikonov S., Gurianov D., Filippov A., Dobrovolsky A., Kolubaev E., Tarasov S. Aluminum Bronze/Udimet 500 composites prepared by electron-beam additive double-wire-feed manufacturing. *Materials*, 2022, vol. 15 (18), p. 6270. DOI: 10.3390/ma15186270.

16. Zykova A.P., Panfilov A.O., Chumaevskii A.V., Vorontsov A.V., Tarasov S.Yu. Electron beam additive manufacturing of composite alloy from stainless steel and aluminum bronze: Microstructure and mechanical properties. *Izvestiya. Ferrous Metallurgy*, 2023, vol. 66 (2), pp. 197–205. DOI: 10.17073/0368-0797-2023-2-197-205.

17. Vorontsov A., Astafurov S., Melnikov E., Moskvina V., Kolubaev E., Astafurova E. The microstructure, phase composition and tensile properties of austenitic stainless steel in a wire-feed electron beam melting combined with ultrasonic vibration. *Materials Science and Engineering: A*, 2021, vol. 820, p. 141519. DOI: 10.1016/j.msea.2021.141519.

18. Ravichandran R., Nanjundan S., Rajendran N. Effect of benzotriazole derivatives on the corrosion and dezincification of brass in neutral chloride solution. *Journal of Applied Electrochemistry*, 2004, vol. 34, pp. 1171–1176. DOI: 10.1007/s10800-004-1702-4.

19. Bard A.J., Parsons R., Jordan J., eds. *Standard potentials in aqueous solution*. New York, CRC Press, 1985. 366 p.

20. Stern M., Geary A.L. Electrochemical Polarization: I. A Theoretical Analysis of the Shape of Polarization Curves. *Journal of the Electrochemical Society*, 1957, vol. 104, pp. 33–63. DOI: 10.1149/1.2428496.

21. Alaneme K.K., Odoni B.U. Mechanical properties, wear and corrosion behavior of copper matrix composites reinforced with steel machining chips. *Engineering Science and Technology, an International Journal*, 2016, vol. 19 (3), pp. 1593–1599. DOI: 10.1016/j.jestch.2016.04.006.

22. Yan Y., Hua W., Zhong S., Zhang L., Dai L., Zhou H., Wu L., Cai L. Electrochemical study of the corrosion behavior of bronze under acetic acid-containing thin electrolyte layers. *Materials Research Express*, 2019, vol. 6, p.0965b7. DOI: 10.1088/2053-1591/ab1545.

23. Takaloo A.V., Daroonparvar M.R., Atabaki M.M., Mokhtar K. Corrosion behavior of heat-treated nickel-aluminum bronze alloy in artificial seawater. *Materials Sciences and Applications*, 2011, vol. 2, pp. 1542–1555. DOI: 10.4236/msa.2011.211207.

Conflicts of Interest

The authors declare no conflict of interest.